Photocatalytic Degradation of Atrazine by Boron-Doped TiO_2 with a Tunable Rutile/Anatase Ratio

Wei-Kang Wang[†], Jie-Jie Chen[†], Miao Gao, Yu-Xi Huang, Xing Zhang[*], Han-Qing Yu[*]

CAS Key Laboratory of Urban Pollutant Conversion, Department of Chemistry, University of Science & Technology of China, Hefei, 230026, China

[†] These authors contributed equally.

*** Corresponding authors:**

Dr. Xing Zhang, Fax: +86-551-63601592; E-mail: zhx0610@ustc.edu.cn

Prof. Han-Qing Yu, Fax: +86-551-63601592; E-mail: hqyu@ustc.edu.cn

Abstract

Atrazine is a widely used herbicide and a typical toxic pollutant. TiO_2-mediated photocatalysis is an efficient way to degrade such a refractory contaminate. In a photocatalyic process, great charge separation and efficient interparticle electron transfer are highly desired and are usually achieved through element doping and phase-junction optimization. However, in the traditional methods for synthesizing phase-junction TiO_2, high phase transition temperature and appropriate adjustors are always needed. In this work, boron-doped (B-doped) TiO_2 with a tunable anatase/rutile ratio is successfully synthesized for efficient atrazine degradation by using a simple one-step calcination method, which is conducted below phase transition temperature with as-prepared Ti and B mixture as a precursor. The formation of the surface-phase junctions between anatase and rutile nanoparticles enables effective interparticle electron transfer and results in more efficient charge separation. Also, the B-doping serves as charge traps, which are able to mediate oxidative electron transfer. The prepared B-doped TiO_2 exhibits a higher photocatalytic activity for the degradation of atrazine, with a reaction rate of 4 times faster than that of the non-doped counterpart. The photogenerated reactive species and degradation intermediates of atrazine are identified, and the photocatalytic atrazine degradation mechanism is elucidated. This study provides a new approach to prepare phase-junction photocatalysts and demonstrates that the anatase/rutile ratio can be tuned by doping element. Such a "killing two birds with one arrow" strategy could be extended for preparing other photocatalysts for the degradation of various pollutants.

Keywords: Atrazine; B-doped TiO_2; phase-junction; photoacatalytic degradation; Tunable ratio

1. Introduction

Atrazine, a widely used herbicide, has attracted interests because of its wide use in agriculture, high toxicity and slow biodegradation in the environment [1]. Many techniques have been developed to treat atrazine-contaminated water, including microbiological process [2, 3], electrochemical method [4-6], photocatalysis [7, 8], etc. Among them, photocatalysis has given much attention in view of its facility, efficiency, cost effectiveness, and utilization of solar energy.

TiO_2 is an intriguing semiconductor photocatalyst because of its chemical inertness, photostability, and environmentally friendly features. However, undesired recombination of photoexcited carriers and wide band gap (3.2 eV) severely limits its practical application. Doping with other elements, as a simple and feasible approach, has been widely used for TiO_2 modification to improve its photocatalytic activity [9]. In particular, doping of nonmetals seems to be an effective way [10]. Also, it is a promising way to achieve visible light activity of TiO_2 *via* nonmetal element doping, such as N, C, S, P, and halogen atoms. Among them, boron doping has been adopted in electrochemical studies, because it can enhance the electron-accepting capacity of TiO_2 [11]. Boron atom tends to either replace an oxygen atom or sits in the interstitial position. Furthermore, density functional calculations about the electronic structure of the B-doped reveal that the *p* orbital of B is mixed with O 2*p* orbitals, which is responsible for the band gap narrowing [12].

At the same time, phase-junction TiO_2 has received extensive interests to improve

the photocatalytic activity of TiO_2 because phase-junction can be advantageous to the separation of photogenerated electron-hole pairs, thus prolonging the recombination time [13]. Our previous work has demonstrated that the phase-junction TiO_2 with a little a relatively small fraction of rutile content has a favorable photocatalytic activity for pollutant degradation [14].

As shown in a previous study [15], more Cl and/or H_2O could shield positive charges at a relatively high HCl/Ti ratio and serve to lessen the effects of electrostatic stabilization (repulsion) to optimize the phase-junction TiO_2 formation in annealing process. Furthermore, H_3BO_3, which was used as the source of boron added into the synthesis process of phase-junction TiO_2 nanocrystals, might have the same effect as HCl to tune the phase ratio and simultaneously achieve B doping. The currently available routes to synthesize phase-junction TiO_2 need organic reagents, complex processes and templates [16, 17]. It is therefore highly desirable to develop a simple method, which can optimize the doping content and achieve a reasonable anatase/rutile (A/R) ratio to improve the photocatalytic performance.

Herein, B-doped TiO_2 (A/R) nanoparticles were successfully synthesized with H_3BO_3 and Ti^{3+} solution by a one-step annealing method below phase-transition temperature. Two strategies in synergy were adopted to improve the photocatalytic performance of TiO_2 nanoparticles. Systematical characterization was carried out to explore the influence of B doping on the electronic band structures, optical properties, separation and transfer of photogenerated electron-hole pairs in TiO_2 (A/R), and the generation of reactive oxygen species in photocatalysis. Also, the capacity of the

as-prepared B-doped TiO_2 (A/R) as a photocatalyst for the degradation of atrazine under irradiation was evaluated. Furthermore, a plausible mechanism for the photocatalytic atrazine degradation in the B-doped TiO_2 (A/R) and the photocatalytic degradation pathways were elucidated.

2. Materials and Methods

2.1 Synthesis of B-doped TiO_2 (A/R) nanocomposites

All chemicals used in this work were analytical-grade reagents and used without further purification.

The B-doped TiO_2 (A/R) nanocomposites were prepared as follows: a 0.30 mm thick Ti foil (0.6 g Ti) was cleaned with acetone, alcohol and deionized water sequentially, and then added into Teflon-lined stainless autoclaves with 50 mL of effective volume. Then, a mixture of water (20 mL) and concentrated hydrochloric acid (20 mL) was slowly added into the autoclave. After that, the sample was autoclaved at 160 °C for 2 h and then naturally cooled under room temperature to obtain solution [18]. Later, H_3BO_3 of different dosage (0, 15, 30, 60, 120, and 150 mg) was dispersed into 10 mL of as-prepared solution. The as-prepared solutions with different amounts of H_3BO_3 were annealed at 500 °C for 2 h with a heating rate of 5 °C/min in air. The obtained products using different amounts of H_3BO_3 were denoted as B1, B2, B3, B4, B5, and B6.

2.2 Characterization of the photocatalysts

The Power X-ray diffraction (XRD) patterns were obtained by a Rigaku diffractometer (TTR-III, Rigaku Co., Japan), using Cu Kα radiation source (λ=1.541841 Å) at a scan speed of 8°/min to determine the crystal phase of the obtained samples with an accelerating voltage and current of 40 kV and 200 mA, respectively. The morphology and structure of the samples were characterized by a transmission electron microscopy (TEM) (JEM2100, JEOL Inc., Japan). The high-resolution transmission electron microscopy (HRTEM) images were taken on an HRTEM (JEM-2010, JEOL Inc., Japan) at an acceleration voltage of 200 kV. The diffuse reflectance spectra (DRS) of the samples were measured on a UV–vis spectrophotometer (SOLID3700, Shimadzu Co., Japan). The chemical composition was characterized by X-ray photoelectron spectroscopy (PHI 5600 XPS spectroscopy, Ulvac-Phi Co., Japan). Fourier transform infrared spectra (FTIR) were recorded on a Vertex 70 spectrometer (Bruker Co., Germany) under the transmission scheme by using the KBr pellet technique.

2.3 Photocatalytic degradation of atrazine

The photocatalytic degradation of atrazine by all the B-doped TiO_2 samples was performed. 20 mg of non-doped and doped TiO_2 nanoparticles were dispersed in 40-mL atrazine solution (10 mg/L) and stirred in dark for 30 min to establish adsorption-desorption equilibrium between the solution and the catalysts. Later, for the photocatalytic reaction, each pollutant solution was irradiated using a 350 W (15

A) Xenon lamp with a 300 nm cutoff filter (CHF-XM-350W, Beijing Trusttech. Co., China) as the light source. The photocatalytic tests were conducted in a 50-mL beaker with a cold bath. After given time intervals, 1 ml of aqueous solution was filtered out from the reactor vessel.

The atrazine concentration was measured by high-performance liquid chromatography (HPLC-1100, Agilent Inc., USA) with a Hypersil-ODS reversed-phase column and detected at 254 nm using a VWD detector. The mobile phase was a mixture of water and methanol (40:60) delivered at a flow rate of 0.8 $mL \cdot min^{-1}$. The atrazine degradation intermediates were analyzed by liquid chromatography mass spectrometry (LC/MS, 6460, Agilent Inc., USA).

Since •OH can react with terephthalic acid (TA) to generate 2-hydroxy terephthalic acid (TAOH), which emits unique fluorescence at 426 nm [19], significant fluorescent signals associated with TAOH are generated upon the UV-vis light irradiation of the samples suspended in 3 mM TA solution containing 10 mM NaOH for different irradiation times. The hydroxyl radical (•OH) concentration was detected at room temperature by Fluorescence spectrometer (LS 55, Perkin Elmer Inc., USA) with 310 nm as the excitation number.

3. Results and Discussion

3.1 Structural and chemical characteristics of the TiO_2 (A/R) nanocomposites

Figure 1a shows the XRD patterns of the samples with different B doping

136 contents. The crystallized structures for the non-doped and doped samples mainly
137 consist of anatase phase (corresponding to 2Theta=25.4°) and rutile phase
138 (corresponding to 2Theta=27.5°). This shows that two phases of anatase and rutile
139 were present in the TiO_2 nanocomposites. The phase contents of the samples can be
140 estimated from the XRD peak intensities with the following equations [20]:

141 $$f_A = \frac{1}{1 + \frac{1}{K}\frac{I_R}{I_A}} \quad (1)$$

142 $$K = 0.79, \text{ if } f_A > 0.2;$$

143 $$K = 0.68, \text{ if } f_A \leq 0.2.$$

144 where f_A is the fraction of anatase phase in the powder, and I_A and I_R are the X-ray
145 intensities of the anatase (101) and rutile (110) diffraction peak, respectively. The
146 weight percentages of rutile in the six samples were estimated to be 51.8, 12.6, 20.9,
147 17.5, 10.3 and 7.5 wt%, respectively. Furthermore, compared with the non-doped, the
148 XRD pattern shows that the rutile content of the samples B2-B6 deceased and the
149 main peak locations of anatase and rutile appeared to shift to a certain degree with B
150 doping.

151 Our previous studies have demonstrated that a relatively high HCl/Ti ratio in the
152 solution could lessen the effects of electrostatic repulsion, which would be hazardous
153 to the formation of rutile [14, 21]. In addition, the presence of H_3BO_3 introduced
154 electrostatic attraction, further promoting the formation of anatase phase. Therefore,
155 the TiO_2 phases are tuned by the synergistic effects of HCl and H_3BO_3.

156 The FTIR spectra of the B-doped TiO_2 (**Figure 1b**) could be validated by the IR

157 finger band below 1000 cm^{-1}, characteristic of the Ti-O-Ti network, and the three
158 intense signals at 1190, 1400, and 1620 cm^{-1}. There is an obvious evolution from two
159 peaks at 694 and 500 cm^{-1} to a single peak at 690 cm^{-1}, as indicated by P1 and P2. To
160 understand the origin of the two peaks, the IR spectra of the two-phase mixed TiO_2
161 was examined. The referenced anatase TiO_2 has one peak at 694 cm^{-1}, and the rutile
162 TiO_2 has two peaks at 656 and 528 cm^{-1}. Thus, the peak at 525 cm^{-1} of the samples in
163 **Figure 1b** was from rutile TiO_2 and the gradually predominant peak at 664 cm^{-1} was
164 attributed to the integrated anatase and rutile structure [22].

165 Apart from 1000 cm^{-1} below, the three intense signals at 1190, 1400, and 1620
166 cm^{-1} were observed. The vibrational band at 1620 cm^{-1} may be unambiguously
167 assigned to the surface-adsorbed water and hydroxyl groups (denoted as b3). The
168 band at 1400 cm^{-1} might be ascribed to the presence of tri-coordinated (in the form of
169 B 3p) interstitial boron (denoted as b2), which tends to interact with ambient oxygen
170 atoms to exhibit chemical environments similar to that of normal Ti-O-B, whereas the
171 band at 1190 cm^{-1} should be attributed to the stretching vibrations of the B-O bonds
172 (denoted as b1) [23]. Such an observation is in good agreement with the XRD results.
173 Briefly, the afore-discussed FTIR results reveal that the boron species in the B-doped
174 TiO_2 mainly were present as trico-ordinated interstitial B and 'boroxol rings'.
175 Nevertheless, the existence of oxygen-substituted B could not be ruled out.

176 In addition to the FTIR spectra analysis, XPS was also used to explore the
177 chemical state of the dopant species incorporated into the TiO_2 lattice. The core level
178 energies of B 1s, O 1s, and Ti 2p of the sample B5 are shown in **Figure 2a**. The B 1s

XPS spectrum could be used to identify the boron species on the surface of the doped TiO_2. As shown in **Figure 2b**, the B 1s XPS spectrum of the B-doped TiO_2 exhibited the typical asymmetrical broad peak in the range of 191.0-195.0 eV, which might be de convoluted (carried out by the XPS PEAK41 software package) into two overlapped peaks centered at 192.6 and 193.3 eV. The former peak at 192.6 eV could be ascribed to interstitial boron, and the peak at 193.3 eV should be attributed to signal originated from $BO_{3/2}$ polymer and/or surface $BO_{3/2}$ species [12, 23]. Similar assignments could also be made for the B from the FTIR spectra analysis. Furthermore, compared with $BO_{3/2}$ species, spectral analyses revealed that the concentrations of the interstitial boron amount to more of the total boron B-doped TiO_2 in agreement with FTIR spectra analysis.

Furthermore, the Ti $2p_{3/2}$ XPS spectrum of the B-doped TiO_2 exhibited a peak responsible for at 459.0 eV, in addition to the $2p_{1/2}$ peak at 464.7 eV (**Figure 2c**). Moreover, the O 1s (B_2O_3) (**Figure 2d**) had a peak responsible for $BO_{3/2}$ species from the B XPS spectrum.

Figure 3 shows the low magnification TEM images of the B-doped TiO_2 samples fabricated at different H_3BO_3 concentrations. The controlled nanocomposite (B1) had many nanorods. With increasing B-doped content, the obtained samples had many nanoparticles along with occasional nanorods. All these samples show similar morphologies, i.e., aggregates of TiO_2 nanoparticles and nanorods with different sizes.

In order to provide direct evidence to support the existence of anatase and rutile phases, the synthesized B-doped TiO_2 samples were further subjected to HRTEM

analysis. **Figure 4** shows the HRTEM images of B5. The lattice spacing of 0.32 nm, which corresponds to the (110) plane of the rutile lattice, was clearly observed. In addition, the lattice spacing of neighbor nanoparticle was 0.35 nm, which corresponds to the (101) plane of the anatase lattice. Therefore, the HRTEM results further confirm the co-existence of the rutile and anatase phases in the TiO_2 nanocomposites. Moreover, the phase-junction between rutile and anatase nanoparticles could be clearly seen from the HRTEM image.

3.2 Photophysical properties of the TiO_2 (A/R) nanocomposites

The optical absorption properties of semiconductor materials are associated strongly with their electronic band structures. The effects of boron doping on the light absorption characteristics of TiO_2 nanoparticles are shown in **Figure 5**. The insert chart in **Figure 5** is the enlarged figure at 350~425 nm. The absorption edge position of all B-doped TiO_2 exhibited a large blue shift, implying that the band gap of B-doped TiO_2 increased because of the much larger band gap of BO_x than TiO_2. This is because the doped boron ion was situated in the interstitial TiO_2 structure, forming a possible chemical environment such as Ti-O-B [24, 25]. On the other hand, a blue-shift of UV-vis absorption edge might be caused due to the reduction of the rutile content by doping [26]. Thus, the B-doped TiO_2 absorbance was attributed to the coupling effects of the rutile and boron contents. This could be used to explain why B2 had a more blue shift compared with B3 and B4. In addition, compared with non-doped TiO_2, the optical absorption intensity of the B-doped TiO_2 nanocomposites

223 was enhanced [27]. This resulted in their improved photocatalytic activity in the
224 UV-vis region.
225
226 **3.3 Photocatalytic atrazine degradation performance**
227 To evaluate the photoactivity of the B-doped TiO_2 samples, photocatalytic
228 experiments for the degradation of atrazine were conducted (**Figure 6**). The blank
229 control (without photocatalyst) showed a stable concentration of atrazine under
230 UV-vis light irradiation. The presence of the B-doped TiO_2 samples resulted in a rapid
231 decrease in atrazine concentration, and the highest atrazine degradation efficiency
232 (94.7%) was achieved by B5 during 180-min light irradiation. The non-doped TiO_2
233 samples showed the total atrazine photodegradation of only 50.1%. For all samples,
234 the photodegradation of atrazine increased substantially with the decreasing rutile
235 amount to 11.6 wt%. This result suggests that the rutile-anatase ratio plays a vital role
236 in governing the recombination of photogenerated h^+/e^- pairs for the two-phase mixed
237 TiO_2, and affecting its photocatalytic activity.
238 The atrazine photodegradation process over time by B5 in **Figure 6c** shows that
239 the intermediates (retention time of 3~6 min) began to accumulate, and then declined
240 owing to the greater degradation rate than the accumulation one. **Figure 6b** illustrates
241 the atrazine photodegradation process over time, which follows the pseudo-first-order
242 kinetics owing to the intermediates degradation process [28]. Therefore, the apparent
243 degradation rate constant (k) of atrazine could be calculated from the slope of the
244 $\ln(C/C_0)$ versus time fitting line, in which C represents the atrazine concentration. A

245 comparison of the atrazine degradation rate constants with different photocatalysts
246 reveals that the fastest atrazine degradation was achieved by the two-phase mixed
247 TiO_2. In addition, k_{B5} was larger than the others in absolute value, suggesting that the
248 optimal B-doped content in the phase-junction TiO_2 was favorable for enhancing the
249 photocatalytic degradation capability.

250 In the photocatalytic reaction, TiO_2 absorbs light to produce electron-hole pairs,
251 which migrate to catalyst surface to react with absorbed O_2 and H_2O, to produce
252 strong oxidizing agents in the form of •OH radicals. •OH radicals are the main species
253 responsible for the degradation of organic pollutants. The results shown in **Figure 6d**
254 clearly show that the generated holes in the newly formed valence bands caused by
255 B-doping could be readily transferred to the surface adsorbed water and hydroxyl
256 groups of the doped TiO_2 to generate •OH radicals. The good linear relationship
257 between fluorescence intensity and irradiation time indicates the stability of the
258 homogeneous B-doped TiO_2. In addition to the dominant route of holes attacking
259 water or hydroxyl groups, there was possible another route to produce hydroxyl
260 radicals by the subsequent reactions.

261 LC/MS analysis was further used to monitor the degradation intermediates to
262 explore the photocatalytic degradation pathways of atrazine by B-doped TiO_2 (A/R).
263 With our experimental results and literature reports [29-31], the various degradation
264 pathways of atrazine by B-doped TiO_2 (A/R) are proposed (**Figure 7**) and described
265 below:

266 2-Hydroxyatrazine, 2-Chloro-4-ethylamino-6-(1-methyl-1-ethanol)

amino-1,3,5-triazine, and desethyldesisopropyl atrazine could not be found in the LC/MS analysis because of their lower concentration or unstablilty.

Ammeline (3.70 min), 2-Hydroxydesethyl atrazine (4.36 min), 2-Chloro-4-amino-6-hydroxy-1,3,5-triazine (4.61 min), 2-Hydroxy-4-acetamido-6-amino-1,3,5-triazine (5.15 min), 2,4-diamino-6-chloro-N-ethyl-1,3,5-triazine (6.09 min), 2,4-diamino-6-chloro-N-(1-methylethyl)-1,3,5-triazine (8.70 min), 2-Chloro-4-acetamido-6-isopropylamino-1,3,5-triazine (13.53 min), and atrazine (26.88 min) were detected in the LC-MS analysis (**Table 2**). These results are in good agreement with those reported previously [29, 30].

3.4 Photocatalytic atrazine degradation mechanisms by TiO_2 (A/R) nanocomposites

Three reasons might be mainly responsible for the improved photocatalytic efficiency of the optimal B-doped TiO_2 (A/R)-B5. Firstly, the phase-junction formed between the anatase nanoparticles and rutile nanoparticles could greatly enhance the photocatalytic activity for photocatalytic activity [32, 33]. The presence of phase-junction is beneficial for the separation of photoinduced charge-carriers (pairs of e^- and h^+) and is responsible for the high photocatalytic activity [32]. It is well known that photocatalysis over TiO_2 (or other semiconductors) is usually considered to be initiated upon absorbing a photon whose energy is greater than the band gap energy and generating photoexcited electron–hole pairs. This band alignment, as

289 shown in **Figure 8**, could favor the transfer of photogenerated electrons from rutile to
290 anatase, and the transfer of holes from anatase to rutile at a clean interface [34].

291 Secondly, the capture position of the carriers also increases with the increasing
292 content of dopant B. Such an increase extends the life of the photogenerated carriers,
293 and favors the photogenerated electron-hole separation. Moreover, the surface B
294 favors the electron-hole pairs with the adsorbed water to generate •OH radicals in the
295 photocatalytic process.

296 Compared with the non-doped TiO_2, the B-doped TiO_2 (A/R) can greatly increase
297 the photocatalyitc oxidation activity of TiO_2 by shifting valence band to positive,
298 which favors the •OH radical formation [35, 36]. It is well known that the presence of
299 surface hydroxyl groups is advantageous to photocatalytic activity because of their
300 ability to mediate oxidative electron transfer. After the irradiation, the conduction
301 band produces a photoinduced electron, while the interstitial B acts as shallow traps
302 for electrons to prolong the life of the photoinduced charge-carriers (pairs of e^- and
303 h^+), as illustrated by Process II in **Figure 7**. This process is essential to improve the
304 UV-vis light catalytic activity of the B-doped TiO_2.

305 Finally, the pairs of e^- and h^+ may diffuse to the surface of the photocatalyst and
306 continue to react with the hydroxyl groups, adsorbed water and oxygen, forming
307 highly active oxidant •OH. Meanwhile, the surface boron species might also introduce
308 Brønsted and Lewis acid centers onto the surfaces of the B-doped TiO_2 [23]. This also
309 is beneficial to improving the photocatalytic activity of TiO_2.

310 All the above reasons enable the B-doped TiO_2 to be an efficient photocatalyst.

311 Thus, B-doping not only tunes the rutile content of the mixed-phase TiO_2, but also the
312 doping itself enhances the photocatalytic activity.
313
314 **4. Conclusions**
315
316 By using a one-step calcination method below phase transition temperature with
317 as-prepared Ti and B mixture as a precursor, B-doped TiO_2 with a tunable
318 rutile/anatase ratio of is successfully synthesized. Both doping and tunable
319 rutile/anatase ratio are responsible for better charge separation via acting as trapping
320 site and phase-junction. The designed and as-synthesized B-doped TiO_2 (rutile/anatase)
321 exhibits a favorable phase-junction structure and a superior photocatalytic activity for
322 the degradation of atrazine under visible light irradiation with 4 times higher rate than
323 the non-doped TiO_2. This work provides a promising approach to prepare doped TiO_2
324 with a tunable rutile/anatase ratio for other element doping. Our findings also imply
325 promising applications for the TiO_2 (rutile/anatase) photocatalyst in water and
326 wastewater treatment and are useful to apply this catalyst for the degradation of
327 diverse refractory pollutants under visible light irradiation.
328
329 **Acknowledgements**
330 The authors thank the National Science Foundation of China (21590812 and
331 51538011), the Program for Changjiang Scholars and Innovative Research Team in
332 University and the Collaborative Innovation Center of Suzhou Nano Science and

Technology of the Ministry of Education of China for supporting this work.

References

[1] E.A. Pappas, C. Huang, Environ Sci Technol, 42 (2008) 7064-7068.

[2] L.P. Wackett, M.J. Sadowsky, B. Martinez, N. Shapir, Appl Microbiol Biotechnol, 58 (2002) 39-45.

[3] E. Silva, A.M. Fialho, I. Sa-Correia, R.G. Burns, L.J. Shaw, Environ Sci Technol, 38 (2004) 632-637.

[4] X. Chen, X.M. Hu, L. An, N.L. Zhang, D.G. Xia, X. Zuo, X.Y. Wang, Electrocatalysis-Us, 5 (2014) 68-74.

[5] A. Ventura, G. Jacquet, A. Bermond, V. Camel, Water Res, 36 (2002) 3517-3522.

[6] G.R.P. Malpass, D.W. Miwa, S.A.S. Machado, P. Olivi, A.J. Motheo, J Hazard Mater, 137 (2006) 565-572.

[7] H.Z. Chen, S.G. Yang, K. Yu, Y.M. Ju, C. Sun, J Phys Chem A, 115 (2011) 3034-3041.

[8] Z.Q. Gao, S.G. Yang, T. Na, C. Sun, J Hazard Mater, 145 (2007) 424-430.

[9] R. Jaiswal, N. Patel, A. Dashora, R. Fernandes, M. Yadav, R. Edla, R.S. Varma, D.C. Kothari, B.L. Ahuja, A. Miotello, Applied Catalysis B-Environmental, 183 (2016) 242-253.

[10] N. Patel, R. Jaiswal, T. Warang, G. Scarduelli, A. Dashora, B.L. Ahuja, D.C. Kothari, A. Miotello, Appl Catal B: Environ, 150 (2014) 74-81.

[11] Y. Su, S. Han, X. Zhang, X. Chen, L. Lei, Materials Chemistry And Physics, 110

(2008) 239-246.

[12] W. Zhao, W.H. Ma, C.C. Chen, J.C. Zhao, Z.G. Shuai, J Am Chem Soc, 126 (2004) 4782-4783.

[13] J. Liu, X. Yu, Q. Liu, R. Liu, X. Shang, S. Zhang, W. Li, W. Zheng, G. Zhang, H. Cao, Z. Gu, Appl Catal B: Environ, 158–159 (2014) 296-300.

[14] W.K. Wang, J.J. Chen, X. Zhang, Y.X. Huang, W.W. Li, H.Q. Yu, Sci Rep, (2016).

[15] G.H. Li, K.A. Gray, Chem. Mater, 19 (2007) 1143-1146.

[16] M. Zukalova, A. Zukal, L. Kavan, M.K. Nazeeruddin, P. Liska, M. Gratzel, Nano Lett, 5 (2005) 1789-1792.

[17] S.L. Chen, A.J. Wang, C.T. Hu, C. Dai, J.B. Benziger, Aiche J, 58 (2012) 568-572.

[18] W.K. Wang, J.J. Chen, W.W. Li, D.N. Pei, X. Zhang, H.Q. Yu, 7 (2015) 20349-20359.

[19] G. Liu, L.Z. Wang, C.H. Sun, X.X. Yan, X.W. Wang, Z.G. Chen, S.C. Smith, H.M. Cheng, G.Q. Lu, Chem Mater, 21 (2009) 1266-1274.

[20] G.H. Li, C.P. Richter, R.L. Milot, L. Cai, C.A. Schmuttenmaer, R.H. Crabtree, G.W. Brudvig, V.S. Batista, Dalton Trans, (2009) 10078-10085.

[21] W.J. Zheng, X.D. Liu, Z.Y. Yan, L.J. Zhu, Acs Nano, 3 (2009) 115-122.

[22] G. Liu, X.X. Yan, Z.G. Chen, X.W. Wang, L.Z. Wang, G.Q. Lu, H.M. Cheng, J Mater Chem, 19 (2009) 6590-6596.

[23] N.D. Feng, A.M. Zheng, Q.A. Wang, P.P. Ren, X.Z. Gao, S.B. Liu, Z.R. Shen,

377 T.H. Chen, F. Deng, J Phys Chem C, 115 (2011) 2709-2719.
378 [24] D. Chen, D. Yang, Q. Wang, Z.Y. Jiang, Ind Eng Chem Res, 45 (2006)
379 4110-4116.
380 [25] K. Yang, Y. Dai, B.B. Huang, Phys Rev B, 76 (2007).
381 [26] H. Jin, Y. Dai, W. Wei, B. Huang, Journal Of Phys D Appl Phys, 41 (2008).
382 [27] N. Lu, H. Zhao, J. Li, X. Quan, S. Chen, Sep Purif Technol, 62 (2008) 668-673.
383 [28] T.C. An, X.H. Zhu, Y. Xiong, Chemosphere, 46 (2002) 897-903.
384 [29] V. Hequet, C. Gonzalez, P. Le Cloirec, Water Res, 35 (2001) 4253-4260.
385 [30] M. Lackhoff, R. Niessner, Environ Sci Technol, 36 (2002) 5342-5347.
386 [31] B. Balci, N. Oturan, R. Cherrier, M.A. Oturan, Water Res, 43 (2009) 1924-1934.
387 [32] J. Zhang, Q. Xu, Z. Feng, M. Li, C. Li, Angew Chem Int Ed, 47 (2008)
388 1766-1769.
389 [33] W. Kim, T. Tachikawa, G.H. Moon, T. Majima, W. Choi, Angew Chem Int Ed, 53
390 (2014) 14036-14041.
391 [34] D.O. Scanlon, C.W. Dunnill, J. Buckeridge, S.A. Shevlin, A.J. Logsdail, S.M.
392 Woodley, C.R.A. Catlow, M.J. Powell, R.G. Palgrave, I.P. Parkin, G.W. Watson,
393 T.W. Keal, P. Sherwood, A. Walsh, A.A. Sokol, Nat Mater, 12 (2013) 798-801.
394 [35] G. Liu, J. Pan, L.C. Yin, J.T.S. Irvine, F. Li, J. Tan, P. Wormald, H.M. Cheng,
395 Adv Funct Mater, 22 (2012) 3233-3238.
396 [36] T.T. Wu, Y.P. Xie, L.C. Yin, G. Liu, H.M. Cheng, J Phys Chem C, 119 (2015)
397 84-89.

Table 1. Efficiencies and rate constants (k) of atrazine degradation by the catalysts prepared at H_3BO_3 concentrations

Catalyst	Rutile content (wt %)	Degradation efficiency (%)	k (min^{-1})	H_3BO_3 dosage (mg)
B1	51.8	50.0	-0.0038	0
B2	12.6	81.1	-0.0086	15
B3	20.9	77.5	-0.0070	30
B4	17.5	76.6	-0.0073	60
B5	10.3	95.0	-0.0160	120
B6	7.5	78.0	-0.0082	150

Table 2. The intermediates and their retention time in the photocatalytic degradation of atrazine by B-doped TiO_2 (A/R)

Number	Abbr.	Compounds	Detection time (min)
I	ATRAZINE	Atrazine	26.88
II	OHA	2-Hydroxyatrazine	undetected
III	AOHE	2-Chloro-4-acetamindo-6-isopropylamino-1,3,5-triazine	13.53
IV	AOHI1	2-Chloro-4-ethylamino-6-(1-methyl-1-ethanol) amino-1,3,5-triazine	undetected
V	OHOE	2-Hydroxy-4-acetamido-6-isopropylamino-1,3,5-triazine	5.15
VI	DEA	Desethylatriazine	8.70
VII	DIA	Deisopropylatriazine	6.09
VIII	OHDEA	2-Hydroxydesethyl atrazine	4.36
IX	DAA	Desethyldesisopropyl atrazine	undetected
X	AME	2-Hydroxy-4,6-diamino-1,3,5-triazine	3.70
XI	$ClOHNH_2$	2-Chloro-4amino-6-hydroxy-1,3,5-triazine	4.61

Figure Legends

Figure 1. (a) XRD patterns and (b) FTIR spectra of the B-doped TiO_2 (A/R) nanoparticles with different B doping contents: 0 mg (B1), 15 mg (B2), 30 mg (B3), 60 mg (B4), 120 mg (B5), and 150 mg (B6).

Figure 2. XPS spectra of the B-doped TiO_2 (A/R) sample (B5): (a) Survey spectra, (b) B 1s, (c) Ti 2p, and (d) O 1s.

Figure 3. Typical TEM images of the B-doped TiO_2 (A/R) sample: (a) B1, (b) B2, (c) B3, (d) B4, (e) B5, and (f) B6. Scale bar: 60 nm.

Figure 4. HRTEM image of the B-doped TiO_2 (A/R) sample (B5).

Figure 5. UV-vis diffuse reflection spectra of all the TiO_2 (A/R) samples

Figure 6. Photocatalytic degradation (a) and pseudo-first-order kinetic constants (b) of atrazine over all the TiO_2 (A/R) samples under UV-vis light irradiation, (c) HPLC chromatograms during photocatalytic degradation of atrazine with the B-doped TiO_2 (A/R) sample (B5). (d) Time dependence of the fluorescence intensity at 426 nm with all B-doped TiO_2 (A/R).

Figure 7. Proposed mechanism for photocatalytic decomposition of by B-doped TiO_2 (A/R) under UV-vis light irradiation. Compounds I, III, V-VIII, X and XI were experimentally detected.

Figure 8. A proposed valence and conduction band alignment mechanism for the B-doped anatase/rutile interface.

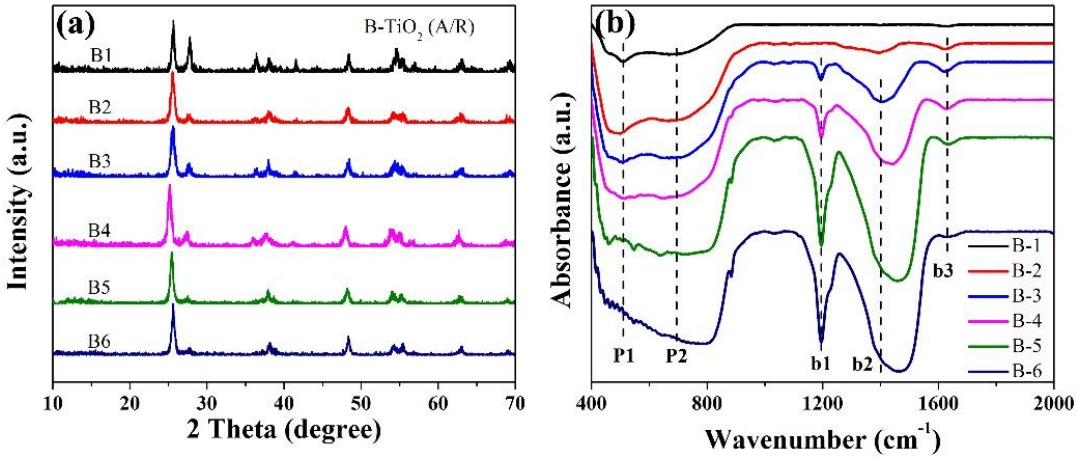
(a)
B-TiO2 (A/R)
B1
B2
B3
B4
B5
B6
Intensity (a.u.)
10
20
30
40
50
60
70
2 Theta (degree)
(b)
Absorbance (a.u.)
P1
P2
b1
b2
b3
B-1
B-2
B-3
B-4
B-5
B-6
400
800
1200
1600
2000
Wavenumber (cm-1)

Figure 1

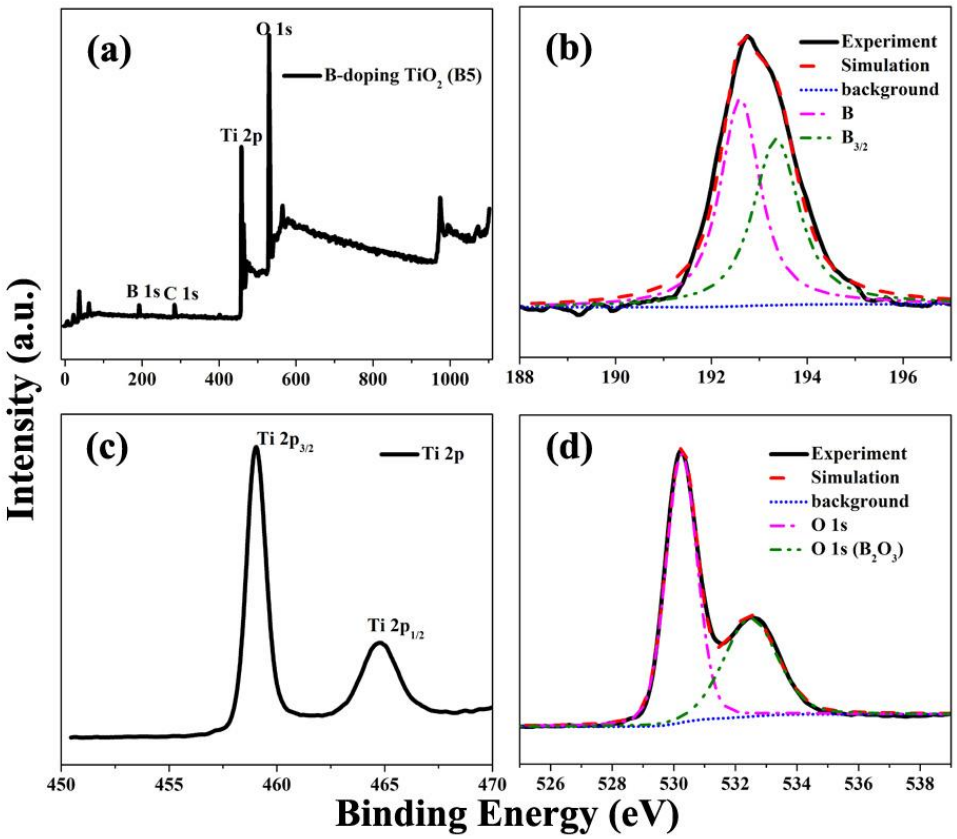
(a)
O 1s
B-doping TiO2 (B5)
Ti 2p
B 1s
C 1s
0
200
400
600
800
1000
(b)
Experiment
Simulation
background
B
B3/2
188
190
192
194
196
(c)
Ti 2p3/2
Ti 2p
Ti 2p1/2
450
455
460
465
470
(d)
Experiment
Simulation
background
O 1s
O 1s (B2O3)
526
528
530
532
534
536
538
Intensity (a.u.)
Binding Energy (eV)

Figure 2

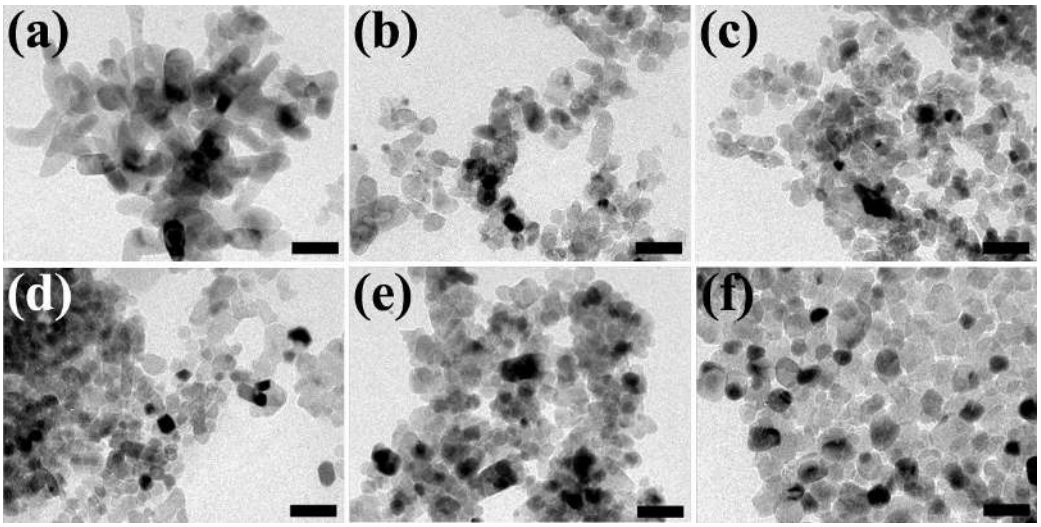

Figure 3

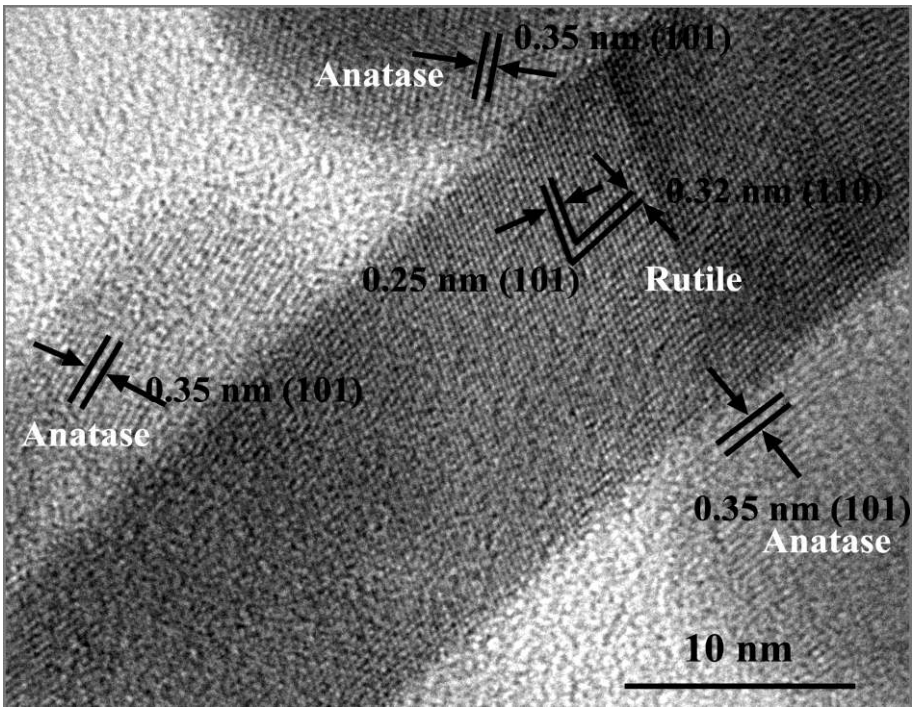
0.35 nm (101)
Anatase
0.32 nm (110)
0.25 nm (101)
Rutile
0.35 nm (101)
Anatase
0.35 nm (101)
Anatase
10 nm

Figure 4

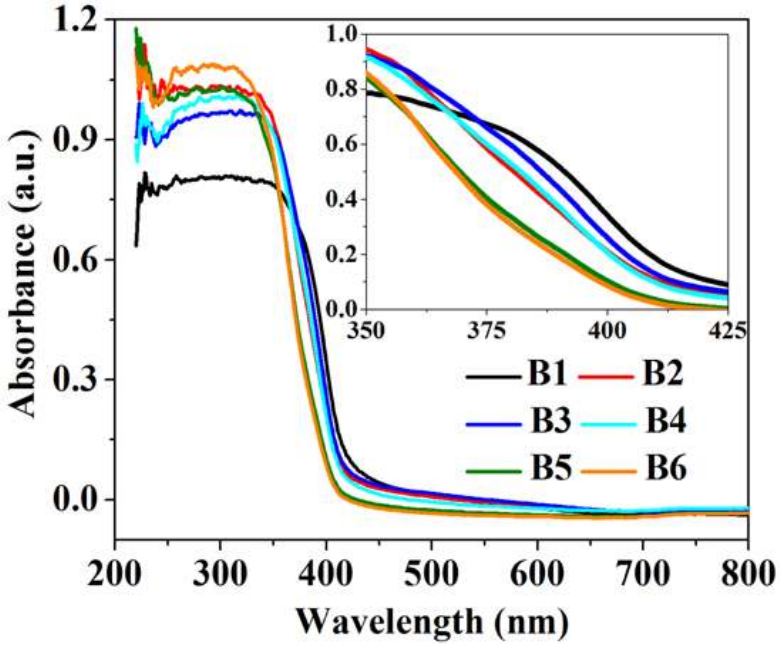

Figure 5

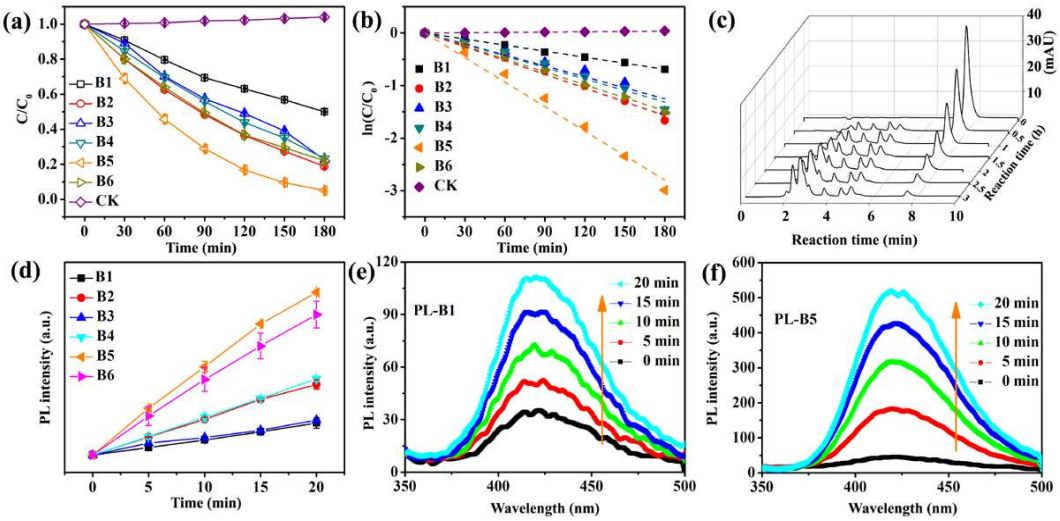
(a)
C/C0
Time (min)
B1
B2
B3
B4
B5
B6
CK
(b)
ln(C/C0)
Time (min)
(c)
Reaction time (min)
Reaction time (h)
(d)
PL intensity (a.u.)
Time (min)
(e)
PL-B1
PL intensity (a.u.)
Wavelength (nm)
20 min
15 min
10 min
5 min
0 min
(f)
PL-B5
PL intensity (a.u.)
Wavelength (nm)

Figure 6

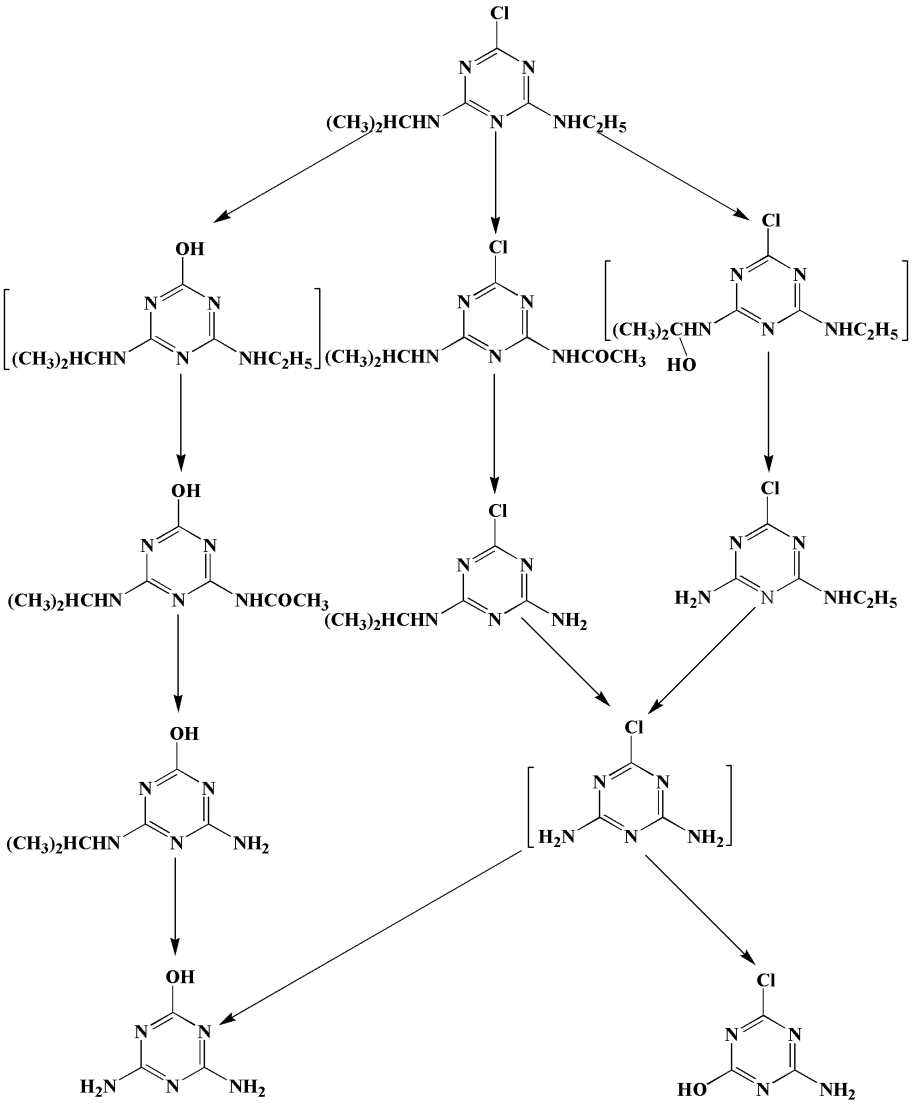
Cl
(CH3)2HCHN
NHC2H5
OH
(CH3)2HCHN
NHC2H5
Cl
(CH3)2HCHN
NHCOCH3
Cl
(CH3)2CHN
HO
NHC2H5
OH
(CH3)2HCHN
NHCOCH3
Cl
(CH3)2HCHN
NH2
Cl
H2N
NHC2H5
OH
(CH3)2HCHN
NH2
Cl
H2N
NH2
OH
H2N
NH2
Cl
HO
NH2

Figure 7

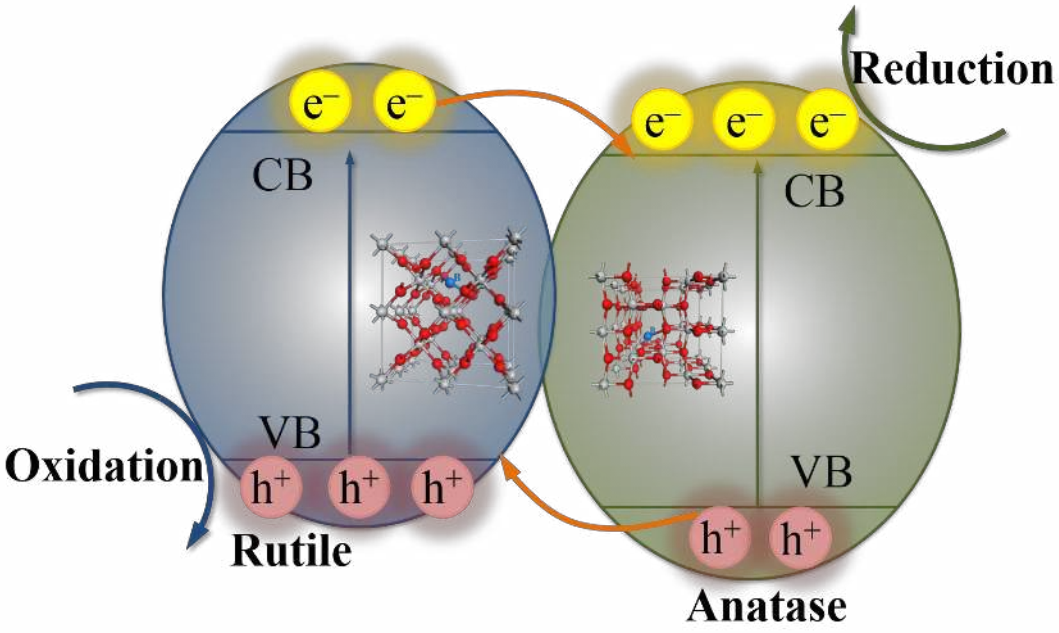

Figure 8

Graphical Abstract